Electronic Supplementary Material (ESI) for Dalton Transactions.
This journal is © The Royal Society of Chemistry 2022

Supplementary Information 1 for

Impact of alkaline-earth doping on electronic properties of the photovoltaic perovskite $CsSnI_3$: Insights from a DFT perspective

I. Ornelas-Cruz[a], I. González[a], J. Pilo[a], A. Trejo[a, *], R. Oviedo-Roa[b, *], M. Cruz-Irisson[a]

[a] Instituto Politécnico Nacional, ESIME-Culhuacán, Av. Santa Ana 1000, 04440 Ciudad de México, México.

[b] Instituto Mexicano del Petróleo, Eje Central Lázaro Cárdenas Norte 152, 07730 Ciudad de México, México.

[*] Corresponding authors: alejandtb13@gmail.com, oviedor@imp.mx

1. Convergence

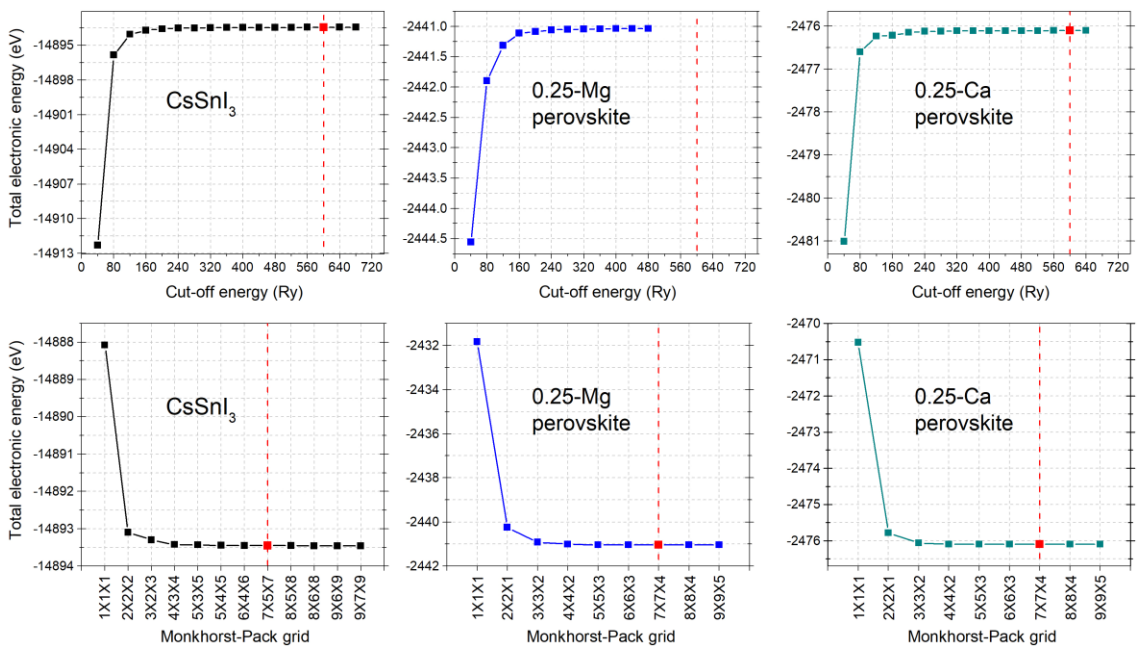

Figure S1. Convergence of the total electronic energy of $CsSnI_3$, MgI_2 and CaI_2 with respect to the cut-off energy (top raw) and to the Monkhorst-Pack grid (lower raw). It was highlighted in red the computational conditions for each case. The cut-off energy employed for MgI_2 and CaI_2 as 600 Ry was employed for all-three structures.

A cut-off energy of 600 Ry was employed for all structures as the energy difference between a previous calculation and the one at issue (600 Ry) was 1.99×10^{-3} eV and $1.81 \times$

10^{-4} eV for $CsSnI_3$ and CaI_3, respectively. For MgI_3 it was not necessary to perform more energy calculations as it was obtained no energy change between the calculation carried out at 440 and 480 Ry.

A *k*-mesh of 7×5×7 was employed for $CsSnI_3$ as there was an energy change between the last calculation of the total electronic energy with a *k*-mesh of 7×5×7 and the previous one with a *k*-mesh of 6×4×6 equal to 5.11×10^{-3} eV (Supplementary Information 2). For both, MgI_2 and CaI_2 a *k*-mesh of 7×7×4 was used as there was an energy change between the calculation at issue (7×7×4) and the previous one with a *k*-mesh of 6×6×3 equal to 1.24×10^{-3} eV and 2.01×10^{-4} eV for MgI_2 and CaI_2, respectively.

2. Optimization of $CsSnI_3$ with dispersion corrections by means of Grimme's approach

Data from the work of Grimme [1] were considered to determine empirically both C_6 (the dispersion coefficient) and R_0 (van der Waal radius) for Cs (see Ref. [1] for more details on these constants). Two functions were fitted from the data for H, Li, Na, K, and Rb to determine C_6; these functions were $A\left(D - B^{-kx^n}\right)$ and $A + Bx + Cx^2 + Dx^3 + Ex^4$ (Supplementary Information 2). For R_0 a linear function, $A + Bx$, was fitted to the data for Li, Na, K, and Rb. The optimized structures (with the same computational conditions of the manuscript's Section 2) were named simply as Grimme1 (C_6 = 466.12 eVÅ^6), Grimme2 (C_6 = 476.20 eVÅ^6), and Grimme3 (C_6 = 486.28 eVÅ^6), distinguished among them by their C_6 value as they all has R_0 = 1.903 Å. Besides, as the Grimme's work suggests s_6 and d were taken as 0.75 and 20, respectively (both being dimensionless parameters). The structural parameters for the unit cell of $CsSnI_3$ after optimization according to methods above described are shown in Table S1 (see at Supplementary Information 2 more structural parameters, such as Sn-I bond lengths or Sn-I-Sn angles).

Table S1. UC parameters for $CsSnI_3$ obtained by using different run conditions. It was indicated within parenthesis the relative error with respect to the experimental values taken from Ref. [2].

UC's parameters	revPBE (as in manuscript)	Grimme1	Grimme2	Grimme3
a (Å)	8.92 (2.71%)	9.20 (5.92%)	9.21 (6.00%)	9.20 (5.91%)
b (Å)	12.55 (1.37%)	12.50 (1.01%)	12.51 (1.06%)	12.50 (1.00%)
c (Å)	8.79 (1.77%)	8.01 (-7.28%)	8.00 (-7.44%)	8.01 (-7.26%)
Volume (Å^3)	984.34 (5.96%)	921.60 (-0.80%)	992.25 (-0.85%)	104.81 (-0.79%)
α (º)	90.00 (0.00%)	90.00 (0.00%)	90.00 (0.00%)	90.00 (0.00%)
β (º)	90.00 (0.00%)	90.00 (0.00%)	89.99 (-0.01%)	90.00 (0.00%)
γ (º)	90.00 (0.00%)	90.00 (0.00%)	90.01 (0.00%)	90.01 (0.01%)

3. Equivalency among the structures of AE-doped perovskites

First, it was necessary to corroborate that the four structures describing AE-doped perovskites in the manuscript's Figure 3, are equivalent among them as expected. Based upon the principles of DFT, for a certain spatial distribution of atoms there is a certain electronic density and, as a consequence, a particular electronic energy [3]. Nevertheless, the equivalency among the optimized structures was demonstrated by means of the calculation of the total electronic energy (E_{DFT}). As Table S1 shows, all the energy differences (ΔE_{DFT}) are in the same order of magnitude than $k_B T$ but for T = 1 K (*i.e.*, $k_B T = 8.6 \times 10^{-5}$ eV). Further, the energy differences computed during the convergence process of the computational parameters (such as *k*-mesh and cut-off energy, see manuscript's Section 2) are one or two orders of magnitude above of all ΔE_{DFT} obtained here. Hence, if one would like to reproduce these results based upon the DFT approach, any of the four structures may jumps up as the most stable one [4].

Table S2. Total electronic DFT energy (E_{DFT}) of each of the four optimized structures for AE-doped perovskites. The energy difference (ΔE_{DFT}) between the structure that obtained the lowest E_{DFT} and each of the remaining ones is also shown. The structures with the lowest E_{DFT} are the structure 3 for the 0.25-Mg perovskites, and structures 3 and 4 for the 0.25-Ca perovskites.

Structure	0.25-Mg perovskite		0.25-Ca perovskite	
	E_{DFT} (eV)	ΔE_{DFT} (eV)	E_{DFT} (eV)	ΔE_{DFT} (eV)
1	-14868.298569	-5.7×10^{-5}	-14903.637488	-0.5×10^{-5}
2	-14868.298597	-2.9×10^{-5}	-14903.637485	-0.8×10^{-5}
3	-14868.298626	0.0	-14903.637493	0.0
4	-14868.298596	-3.0×10^{-5}	-14903.637493	0.0

4. Energies involved in the determination of E_F

Table S3. E_{DFT} of each of the four optimized unit cells of the reactants involved in the formability of the undoped and AE-doped perovskites, and E_{DFT} of the perovskites employed for the calculation of E_F. Z refers to the number of times the unit cell contains the chemical formula at issue. The energy of each reactant employed for the calculation of E_F was the ratio E_{DFT}/Z.

Structures	E_{DFT} (eV)	Z	E_{DFT}/Z (eV)
SnI_2	-14,741.247117	6	-2,456.874520
MgI_2	-2,440.095087	1	-2,440.095087
CaI_2	-2,475.159982	1	-2,475.159982
CsI	-1,264.159732	1	-1,264.159732
$CsSnI_3$	-14,885.67317	4	-3,721.418293
0.25-Mg perovskite	-14,868.298569	4	-3,717.074642
0.25-Ca perovskite	-14,903.637488	4	-3,725.909372

5. Remaining optimized structures and magnified octahedral distortion for 0.25-AE perovskites

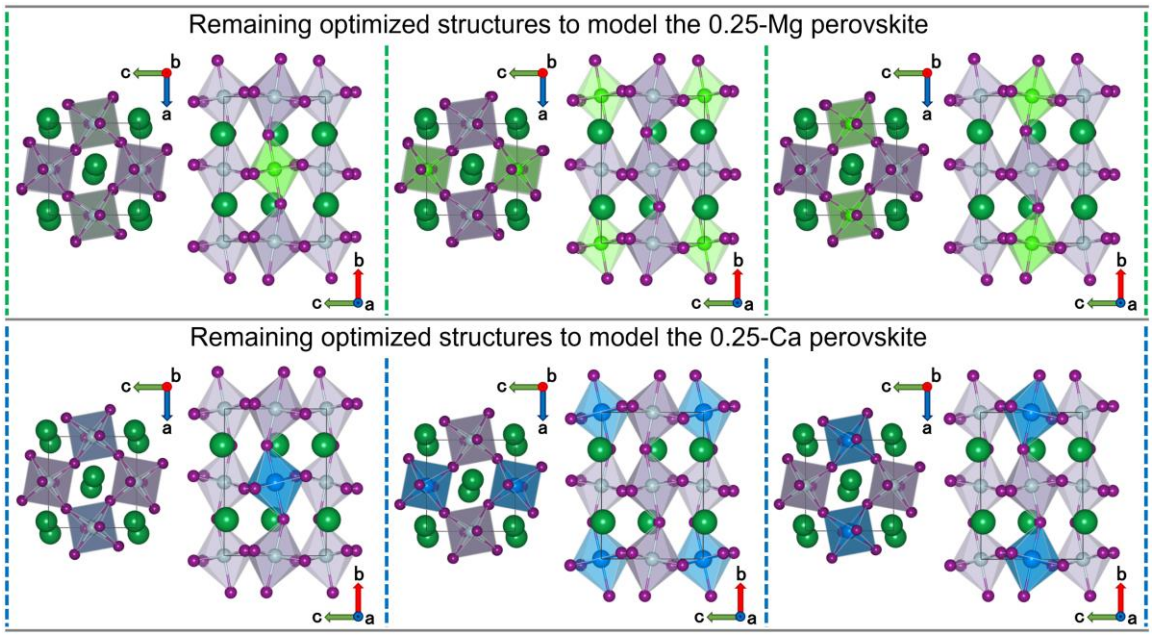

Figure S2. As the main article mentioned, four structures were considered to calculate the averaged values presented in Figure 3, and Table 1 and 2. Here, it is shown the three additional optimized structures employed for the mentioned purpose for both, 0.25-Mg and 0.25-Ca perovskites.

With respect to the angles θ_a, θ_b and θ_c (defined by the manuscript's Equation 3), it is relevant to clarify briefly the relation between these angles and the Glazer notation. Assuming the same frame of reference as in Figure S3, the same $\langle l \rangle$ and $\langle \Phi \rangle$ in all the octahedrons, and the symmetry demanded by the octahedral tilting, in the Glazer tilt pattern $a^0a^0a^0$, for example, both $\langle \theta_a \rangle$ and $\langle \theta_c \rangle$ would be equal to 45°, and $\langle \theta_b \rangle$ would be equal to 0°. Having the octahedral tilting $a^0b^+a^0$ would bring about that both $\langle \theta_a \rangle$ and $\langle \theta_c \rangle$ would be distinct from 45°, in fact, one angle would be reduced and the other one would be increased by the same amount; meanwhile, $\langle \theta_b \rangle$ will still be equal to 0°. Notwithstanding, when an octahedral tilting such as $a^+b^+a^+$ is present in the perovskite, $\langle \theta_b \rangle$ is different from 0°, and, the horizontal plane formed by the vectors $\overrightarrow{v_1}$ and $\overrightarrow{v_2}$ (v_1v_2-plane in Figure S3) is no longer parallel to the plane formed by the UC's vectors $\vec{a}$ and $\vec{c}$ (ac-plane in Figure S3). Meanwhile, the difference between $a^+b^+a^+$ and $a^-b^+a^-$ has to do with the vector $\overrightarrow{v_3}$. If two octahedrons from the same horizontal plane are considered (Figure S3), one located at the ab-plane with vector $\overrightarrow{v_3^{ab}}$ and the other one located in the bc-plane with vector $\overrightarrow{v_3^{bc}}$ (Figure S3), the sum of $\overrightarrow{v_3^{ab}}$ and $\overrightarrow{v_3^{bc}}$ will be a vector $\vec{v}$ parallel to $\vec{b}$ when the octahedral tilting $a^-b^+a^-$ is present in the perovskite. By contrast, when having the Glazer tilt pattern $a^+b^+a^+$, the resultant vector $\vec{v}$ will be unparallel to $\vec{b}$.

Please consider that the above explained is not fulfilled by the 0.25-AE perovskites since there is an inhomogeneity on the tilting and distortion of the octahedrons within these perovskite structures.

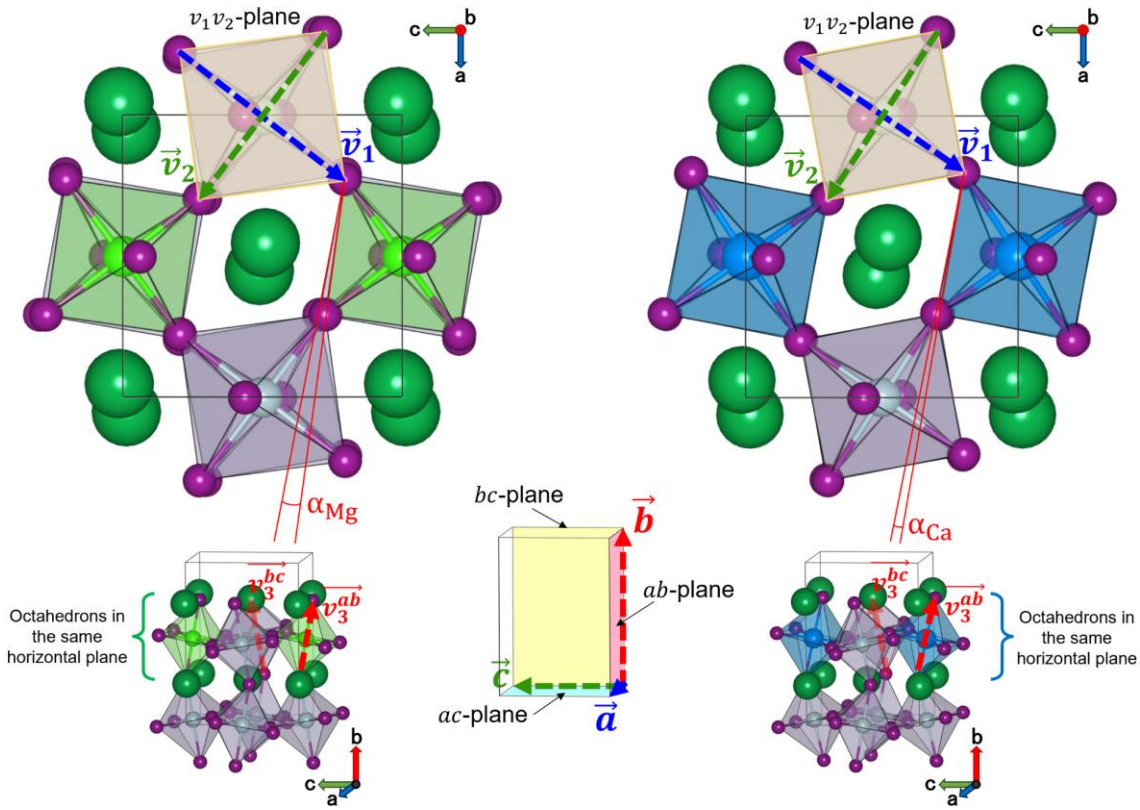

Figure S3. Magnification of the octahedral tilting difference between the AE and Sn octahedrons. The structures are the same shown in Figure 3a of the manuscript, but the upper octahedrons are not shown for convenience in this figure. Both angles, α_{Mg} and α_{Ca}, were not calculated, there were picturized only to show that there are distinct rotations around the vertical axis for the AE and Sn octahedrons pointed out by the averaged values of $\langle\theta_a\rangle$ and $\langle\theta_b\rangle$, as it is mentioned in the manuscript. To understand further the utility of having defined the vectors $\vec{v}_1$, $\vec{v}_2$ and $\vec{v}_3$, please see the text above.

6. Chemical environment of I and Sn within $CsSnI_3$

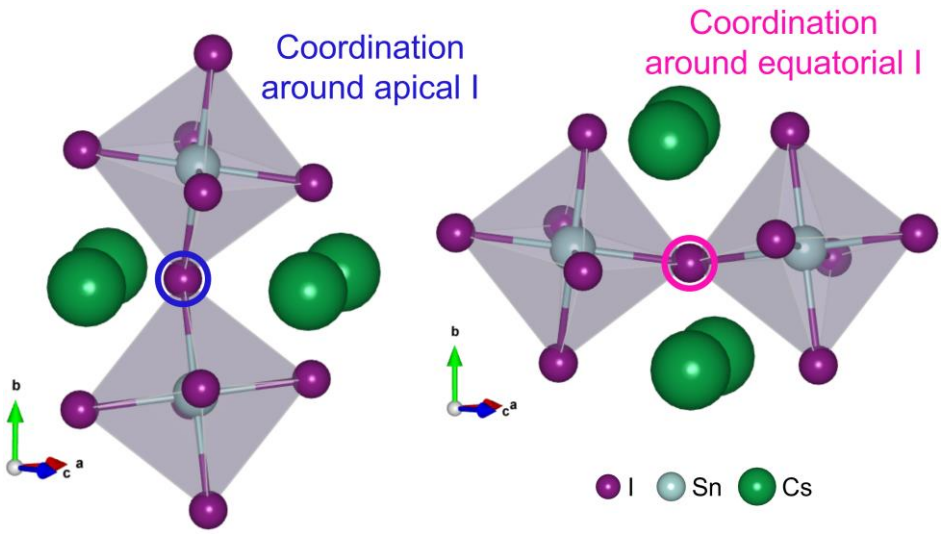

Figure S4. Coordination of apical and equatorial I. Also, it was observed that each Sn atom is surrounded by practically the same conformational environment.

7. Partial COHP curves for the $CsSnI_3$, 0.25-Mg and 0.25-Ca perovskites

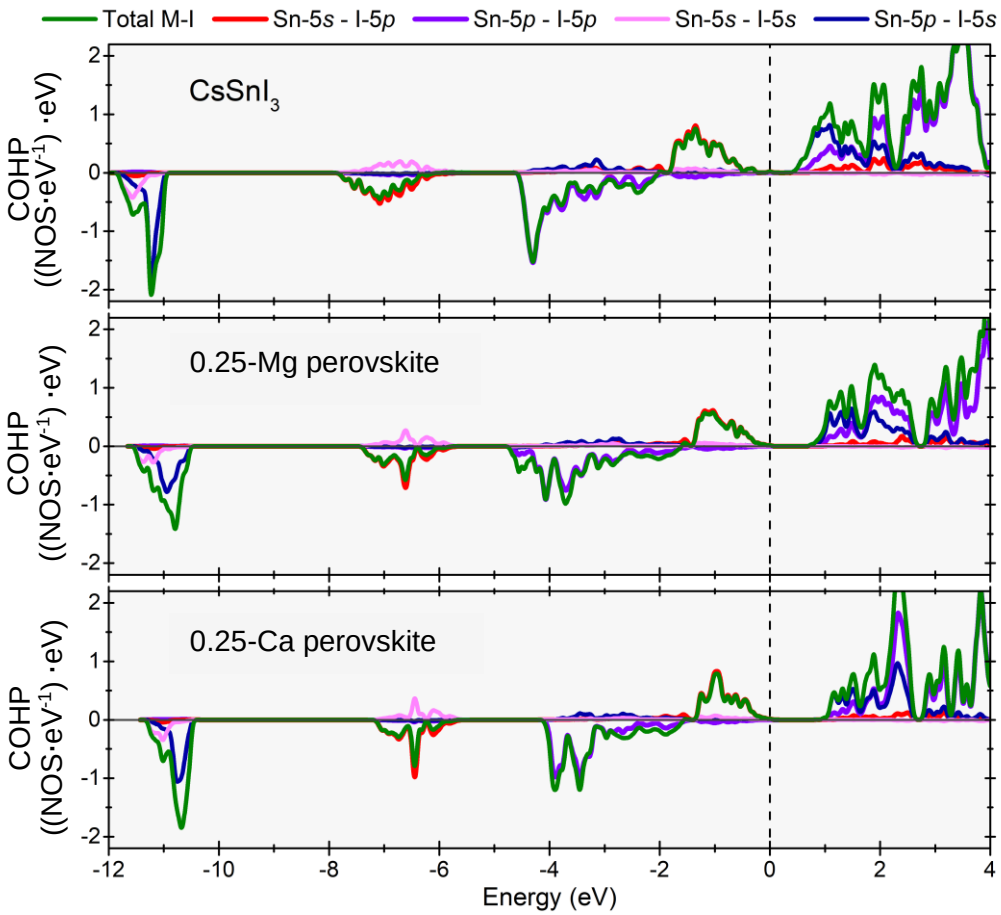

Figure S5. COHP analysis for both Sn-5s and Sn-5*p* orbitals hybridized with both I-5*s* and I-5*p*.

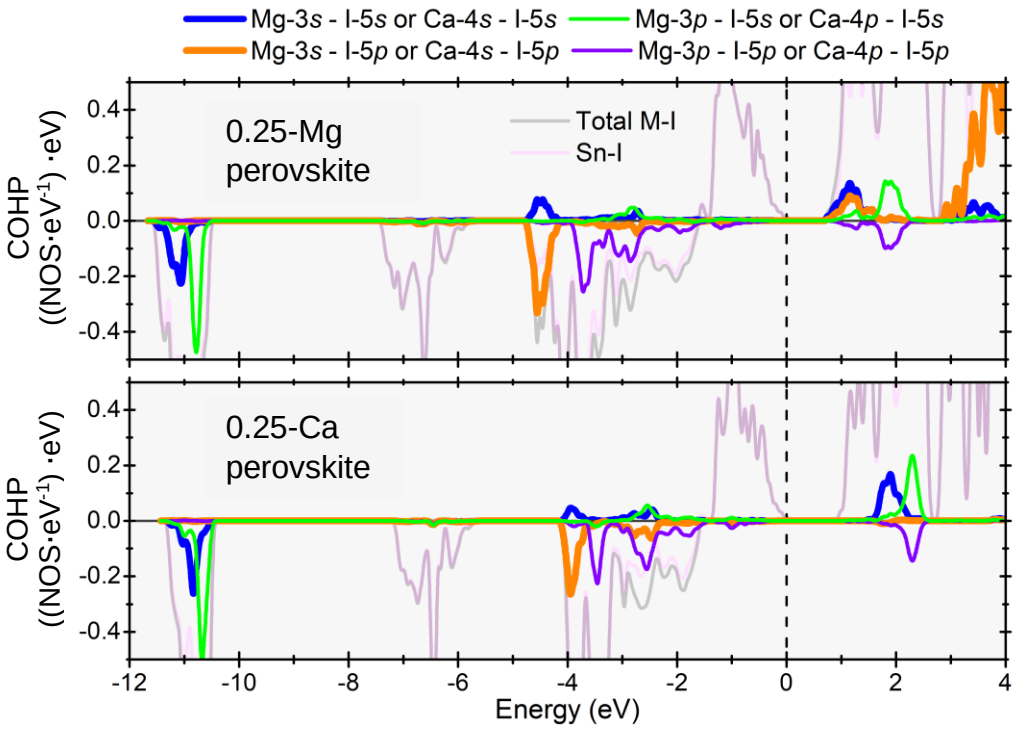

Figure S6. COHP analysis for Mg-3*s*, Mg-3*p*, Ca-4*s* and Ca-4*p* orbitals hybridized with both I-5*s* and I-5*p*.

8. PDOS of the $CsSnI_3$, 0.25-Mg and 0.25-Ca perovskites

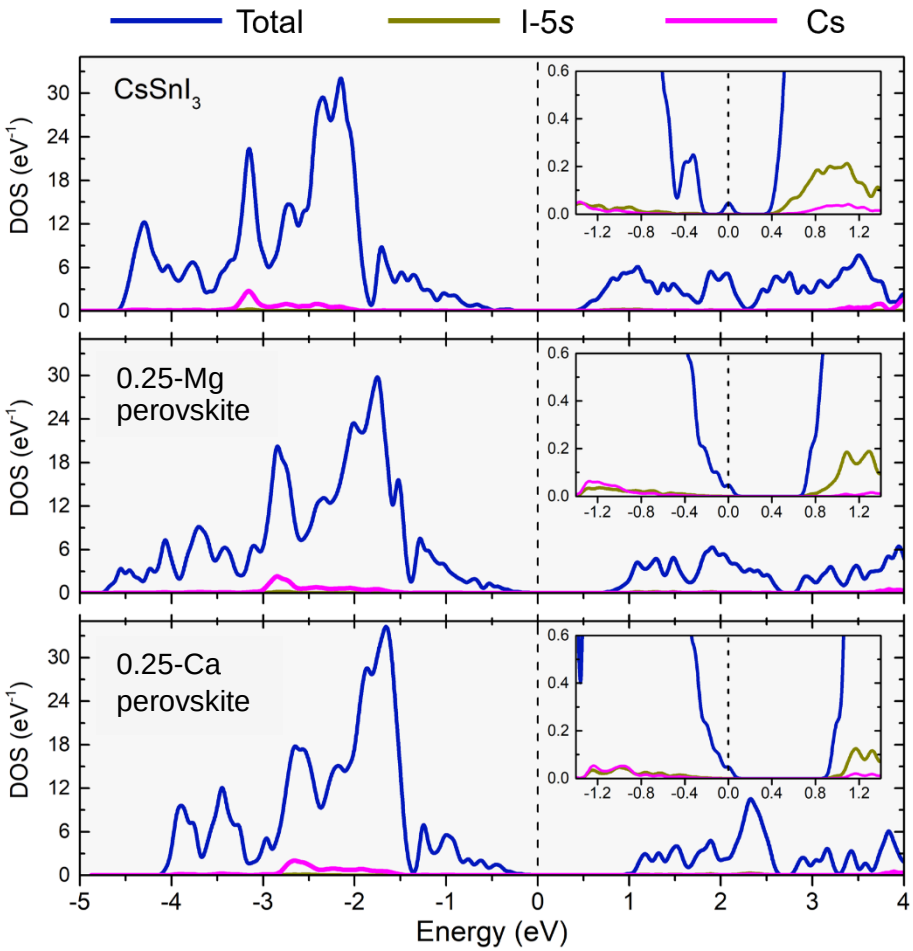

Figure S7. Total density of states (DOS), partial DOS for Cs, and projected partial DOS for I-5*s* for all-three perovskites studied in this work.

9. V_{OC}, V_{MP}, FF and PCE of PSC based on AE-perovskites

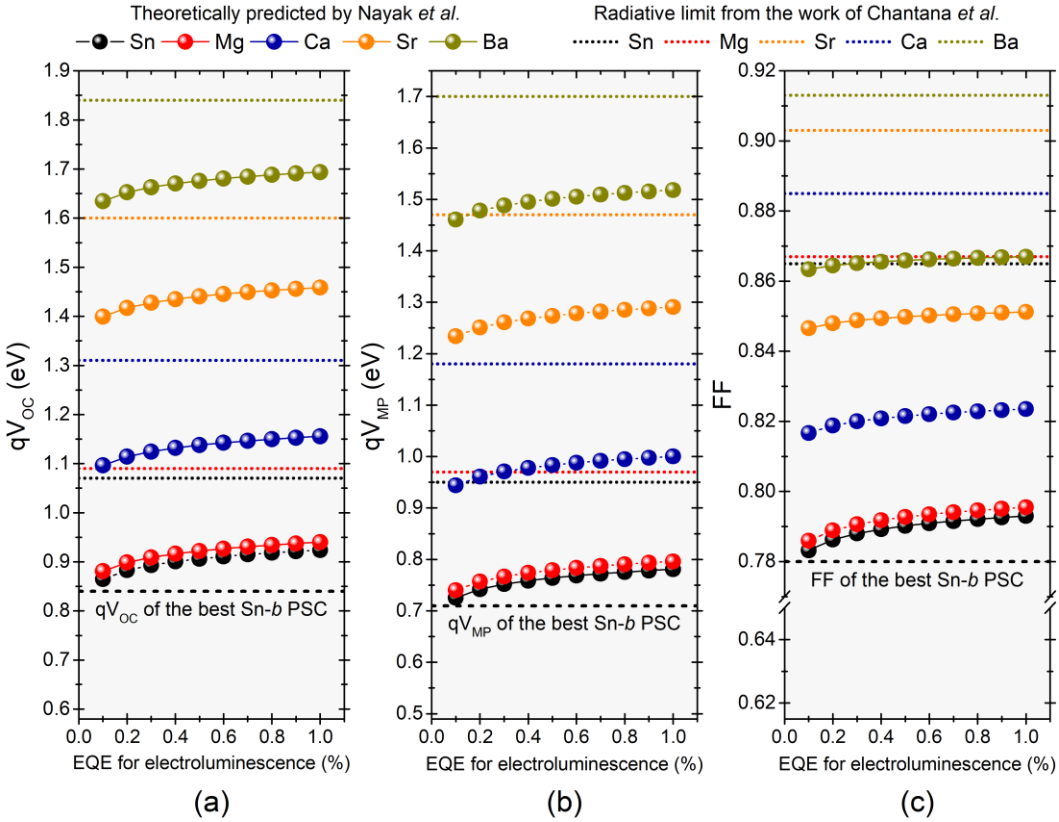

Figure S8. V_{OC}, V_{MP} and FF as a function of the external quantum efficiency (EQE) for electroluminescence. All perovskites are identified by the species occupying the M-site in the chemical formula $CsSn_{0.75}M_{0.25}I_3$. The bandgap energy for $CsSnI_3$ is the experimental one (1.3 eV). The data of the best Sn-*b* PSC was taken from Ref. [5].

Equations S1a, S1b, and S1c were used to calculate V_{OC}, V_{MP} and FF values. All of them were taken from the work of Nayak *et al*. [6].

$$qV_{OC} = 0.941E_g - (0.181 + 0.0257|\ln(\eta_{ext})|) \tag{S1a}$$

$$\frac{qV_{OC}}{nkT} = \frac{qV_{MP}}{nkT} + \ln\left(\frac{qV_{MP}}{nkT} + 1\right) \tag{S1b}$$

$$FF = \frac{\frac{qV_{OC}}{nkT} - \ln\left[\frac{qV_{OC}}{nkT} - \ln\left(\frac{qV_{OC}}{nkT} + 1\right) + 1\right]}{\frac{qV_{OC}}{nkT}} \times \frac{\frac{qV_{OC}}{nkT} - \ln\left(\frac{qV_{OC}}{nkT} + 1\right)}{\frac{qV_{OC}}{nkT} - \ln\left(\frac{qV_{OC}}{nkT} + 1\right) + 1} \tag{S1c}$$

In Equation S1a, E_g and η_{ext} refer to the bandgap energy and the external quantum efficiency (EQE) for electroluminescence, respectively, and q is the elementary charge. In Equations S1b and S1c, n, k, and T are the diode ideality factor, Boltzmann constant, and

the temperature of the solar cell. Originally, Nayak *et al*. [6] used the photovoltaic bandgap ($E_{\mathrm{g}}^{\mathrm{PV}}$) instead of the DFT-determined bandgap energy (E_{g}) of the absorber material, as in the present work; nevertheless, for practical purpose, it was assumed that $E_{\mathrm{g}} = E_{\mathrm{g}}^{\mathrm{PV}}$. Besides, with respect to η_{ext}, the interval $0.1\% \leq \eta_{\mathrm{ext}} \leq 1.0\%$ was considered since for 3D Sn-*b* perovskites it has been reported values of 0.16% and 0.72% for $CsSnBr_3$ [7] and $CH_3NH_3SnI_3$ [8], respectively. In Equations S1b and S1c, it was considered n = 2 as it could be the case for PSC devices [9], and T = 298.15 K. All data shown in Figure S6 were computed in the Supplementary Information 2.

On the other hand, the work of Chantana *et al*. [10] was used to calculate the PCE *in-rad-lim*, referred in its work as the "detailed balance limit". Besides, all three parameters, V_{OC}, V_{MP} and FF, which are required to calculate the PCE *in-rad-lim*, were plotted in Figure S4. Equations S2a to S2f below were considered for this purpose [10].

$$\mathrm{PCE}(E_{\mathrm{g}}) = \frac{\max[J(E_{\mathrm{g}}, V) \cdot V]}{P_{in}} \tag{S2a}$$

$$\mathrm{FF}(E_{\mathrm{g}}) = \frac{\max[J(E_{\mathrm{g}}, V) \cdot V]}{J_{SC}(E_{\mathrm{g}}) \cdot \mathrm{V_{OC}}(E_{\mathrm{g}})} \tag{S2b}$$

$$J_{SC}(E_{\mathrm{g}}) = q \cdot [Q_s(E_{\mathrm{g}})] \tag{S2c}$$

$$J(E_{\mathrm{g}}, V) = q \cdot \left\{Q_s(E_{\mathrm{g}}) - Q_C(E_{\mathrm{g}}) \left[e^{\left(\frac{qV}{kT}\right)} - 1\right]\right\} \tag{S2d}$$

$$Q_s(E_{\mathrm{g}}) = \int_{E_{\mathrm{g}}}^{\infty} \frac{\lambda dE}{[E(\lambda)]^2} \cdot [\mathrm{ASTM\ G173}(\lambda)] \tag{S2e}$$

$$Q_C(E_{\mathrm{g}}) = \frac{2\pi}{h^3 c^2} \int_{E_{\mathrm{g}}}^{\infty} \frac{E^2}{e^{\left(\frac{E}{kT}\right)} - 1} dE \tag{S2f}$$

V becomes V_{MP} after the maximization of the product $J(E_{\mathrm{g}}, V) \cdot V$, and $qV = \mu$, with q and μ being the elementary charge and the quasi-Fermi level splitting, respectively; besides, $J(E_{\mathrm{g}}, V)$ is the current density of the solar cell. k, h, c and T are the Boltzmann constant, Planck constant, speed of light in vacuum, and the temperature of the solar cell, respectively. For the latter, it was considered T = 298.15 K. $J_{SC}(E_{\mathrm{g}})$ and $Q_s(E_{\mathrm{g}})$ are the short-circuit density current and the incident spectral photon flux. $[\mathrm{ASTM\ G173}(\lambda)]$ is the spectral irradiance according to the American Society for Testing and Materials, with a global tilt of 37° as provided by the National Renewable Energy Laboratory (URL: https://www.nrel.gov/grid/solar-resource/spectra-am1.5.html). $Q_C(E_{\mathrm{g}})$ is the photon flux of the spectral irradiance of a blackbody at 298.15 K. All integrals were evaluated from E_{g} up to 4.43 eV (280 nm), and P_{in} is the integration over all the spectrum; thus, P_{in} = 100.03707

mW/cm^2. All values shown in Figure S6 were computed in the Supplementary Information 2.

10.Effective mass

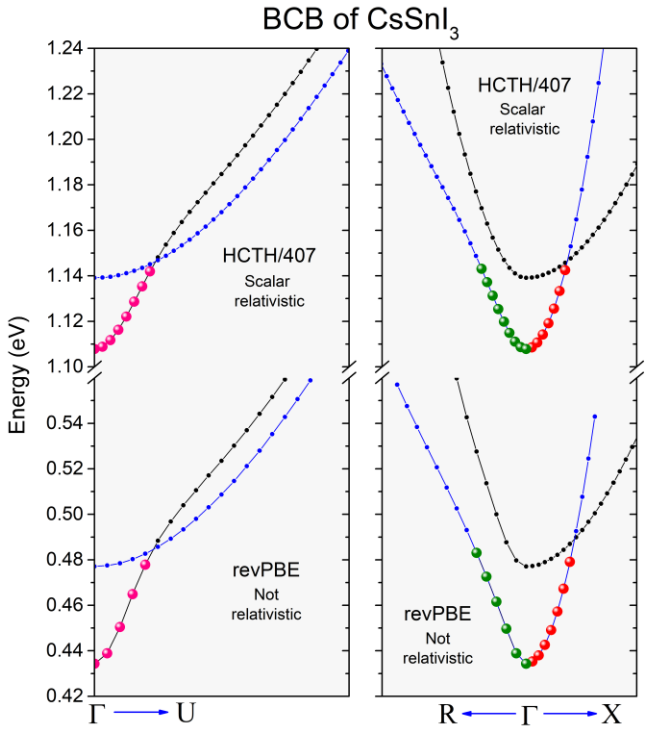

Figure S9. BCB of $CsSnI_3$ perovskite with two different pseudopotentials: the local scalar relativistic one developed by Delley [11] and the non-relativistic norm-conserving Troullier–Martins pseudopotentials [12].

Table S4. Effective masses for holes and electrons within $CsSnI_3$ along three different directions within the first Brillouin zone. "nR" and "SR" refer to non-relativistic and scalar-relativistic corrections, respectively.

Charge	Γ-X		Γ-Y		Γ-Z	
	revPBE (nR)	HCTH/407 (SR)	revPBE (nR)	HCTH/407 (SR)	revPBE (nR)	HCTH/407 (SR)
m_e	1.00	1.02	58.14	31.51	3.09	3.31
m_h	0.50	0.88	4.22	4.52	5.14	4.49

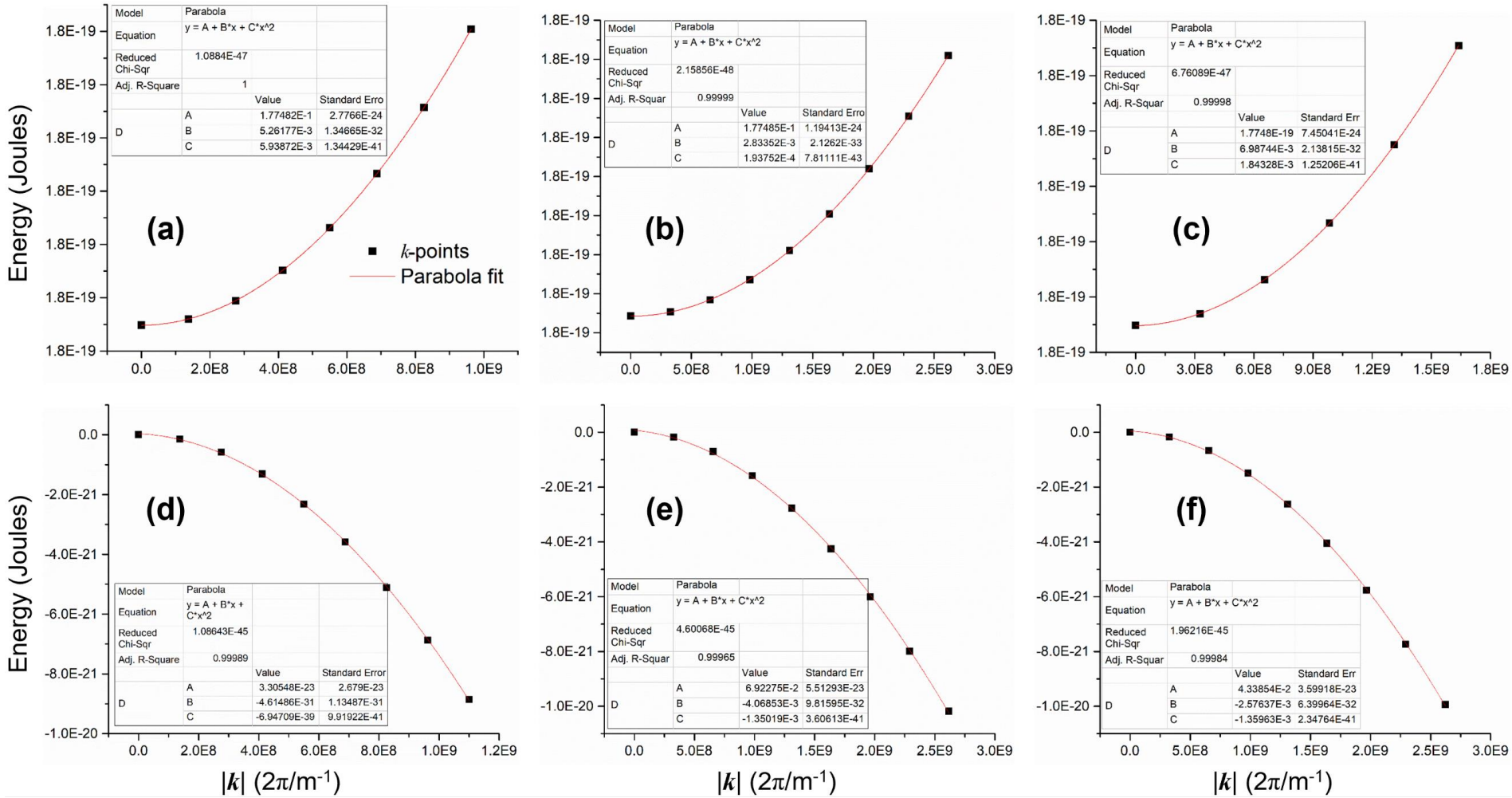

Figure S10. Parabola fit to the *k*-points at the BCB and TVB for $CsSnI_3$ along the directions mentioned in the work. Fits at (a) and (d) were used to calculate the effective masses of the electron and hole, respectively, along the [100] direction. Fits at (b) and (e) were used to calculate the effective masses of the electron and hole, respectively, along the [010] direction. Fits at (c) and (f) were used to calculate the effective masses of the electron and hole, respectively, along the [001] direction. Based on the quadratic approximation and the results presented herein, all effective masses were calculated by means of $m^* = (\hbar^2/2C)/m_e$ where C is the coefficient of the quadratic term, obtained from the inset of each graph, and m_e is the electron rest mass.

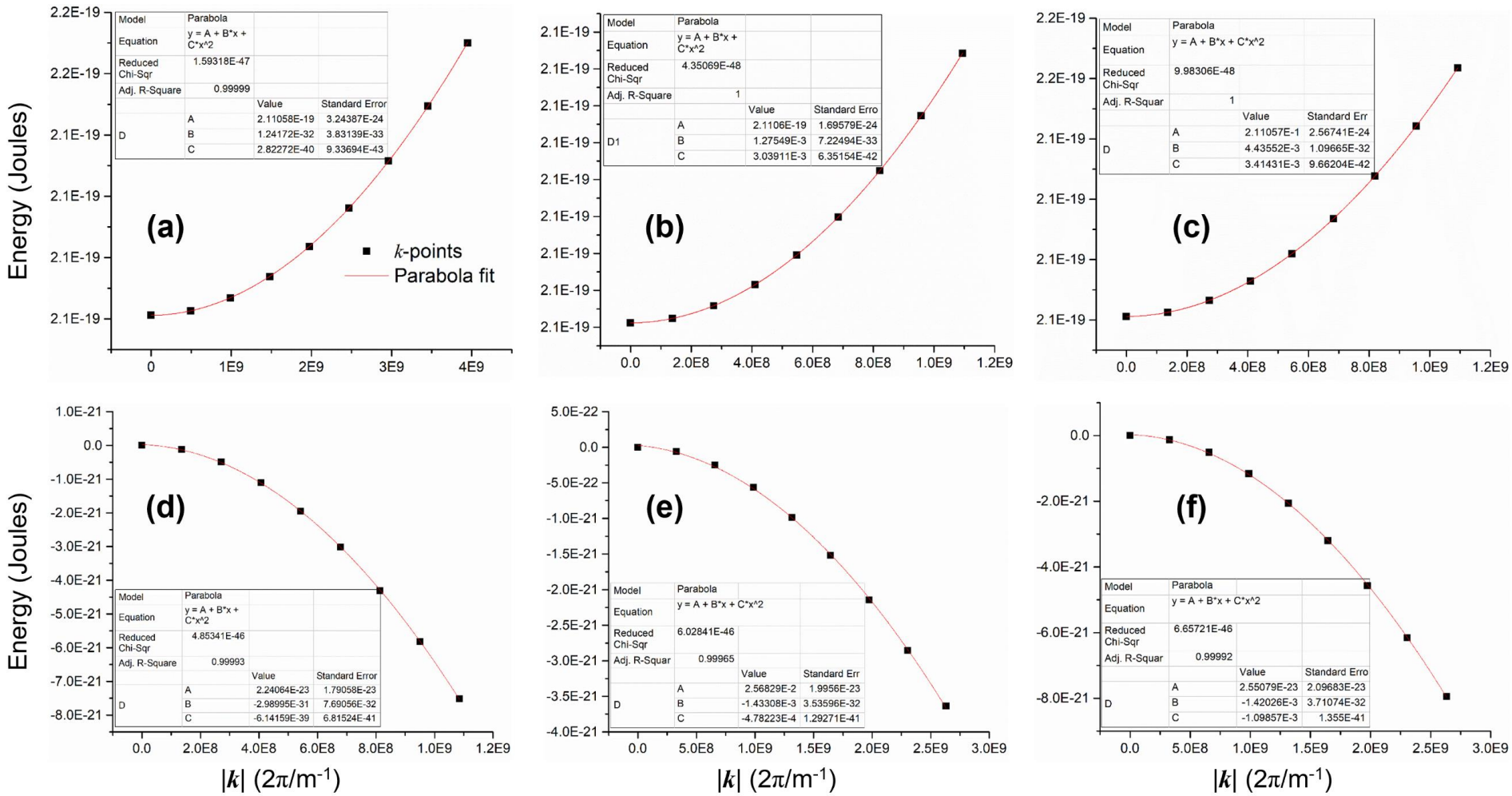

Figure S11. Parabola fit to the *k*-points at the BCB and TVB for the 0.25-Mg perovskite along the directions mentioned in the work. Fits at (a) and (d) were used to calculate the effective masses of the electron and hole, respectively, parallel to the [100] direction. Fits at (b) and (e) were used to calculate the effective masses of the electron and hole, respectively, parallel the [010] direction. Fits at (c) and (f) were used to calculate the effective masses of the electron and hole, respectively, parallel to the [001] direction. Based on the quadratic approximation and the results presented herein, all effective masses were calculated by means of $m^* = (\hbar^2/2\mathrm{C})/m_e$ where C is the coefficient of the quadratic term, obtained from the inset of each graph, and m_e is the electron rest mass.

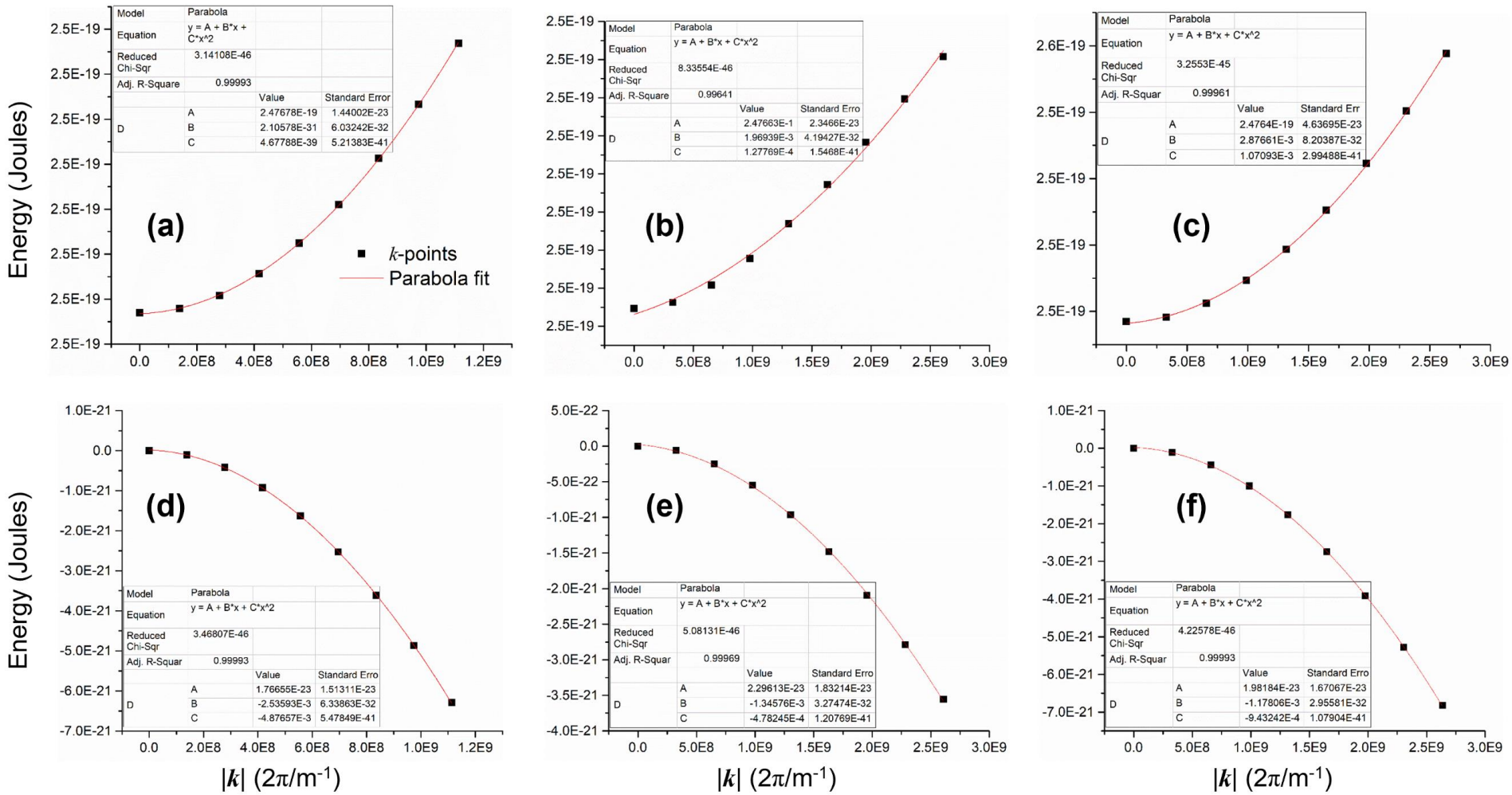

Figure S12. Parabola fit to the *k*-points at the BCB and TVB for the 0.25-Ca perovskite along the directions mentioned in the work. Fits at (a) and (d) were used to calculate the effective masses of the electron and hole, respectively, along the [100] direction. Fits at (b) and (e) were used to calculate the effective masses of the electron and hole, respectively, along the [010] direction. Fits at (c) and (f) were used to calculate the effective masses of the electron and hole, respectively, along the [001] direction. Based on the quadratic approximation and the results presented here, all effective masses were calculated by means of $m^* = (\hbar^2/2\mathrm{C})/m_e$ where C is the coefficient of the quadratic term, obtained from the inset of each graph, and m_e is the electron rest mass.

11.References

[1] → S. Grimme, Semiempirical GGA-type density functional constructed with a long-range dispersion correction, J. Comput. Chem. 27 (2006) 1787–1799. https://doi.org/10.1002/jcc.20495

[2] → I. Chung, J.-H. Song, J. Im, J. Androulakis, C.D. Malliakas, H. Li, A.J. Freeman, J.T. Kenney, M.G. Kanatzidis, CsSnI3: Semiconductor or metal? High electrical conductivity and strong near-infrared photoluminescence from a single material. high hole mobility and phase-transitions, J. Am. Chem. Soc. 134 (2012) 8579–8587. https://doi.org/10.1021/ja301539s.

[3] → F. Giustino, Materials modelling using Density Functional Theory: Properties and predictions, Oxford University Press, New York, NY, 2014.

[4] → K. Lejaeghere, G. Bihlmayer, T. Björkman, P. Blaha, S. Blügel, V. Blum, D. Caliste, I.E. Castelli, S.J. Clark, A. Dal Corso, S. de Gironcoli, T. Deutsch, J.K. Dewhurst, I. Di Marco, C. Draxl, M. Dułak, O. Eriksson, J.A. Flores-Livas, K.F. Garrity, L. Genovese, P. Giannozzi, M. Giantomassi, S. Goedecker, X. Gonze, O. Grånäs, E.K.U. Gross, A. Gulans, F. Gygi, D.R. Hamann, P.J. Hasnip, N.A.W. Holzwarth, D. Iuşan, D.B. Jochym, F. Jollet, D. Jones, G. Kresse, K. Koepernik, E. Küçükbenli, Y.O. Kvashnin, I.L.M. Locht, S. Lubeck, M. Marsman, N. Marzari, U. Nitzsche, L. Nordström, T. Ozaki, L. Paulatto, C.J. Pickard, W. Poelmans, M.I.J. Probert, K. Refson, M. Richter, G.-M. Rignanese, S. Saha, M. Scheffler, M. Schlipf, K. Schwarz, S. Sharma, F. Tavazza, P. Thunström, A. Tkatchenko, M. Torrent, D. Vanderbilt, M.J. van Setten, V. Van Speybroeck, J.M. Wills, J.R. Yates, G.-X. Zhang, S. Cottenier, Reproducibility in density functional theory calculations of solids, Science. 351 (2016) aad3000. https://doi.org/10.1126/science.aad3000.

[5] → K. Nishimura, M.A. Kamarudin, D. Hirotani, K. Hamada, Q. Shen, S. Iikubo, T. Minemoto, K. Yoshino, S. Hayase, Lead-free tin-halide perovskite solar cells with 13% efficiency, Nano Energy. 74 (2020) 104858. https://doi.org/10.1016/j.nanoen.2020.104858

[6] → P.K. Nayak, S. Mahesh, H.J. Snaith, D. Cahen, Photovoltaic solar cell technologies: analysing the state of the art, Nat. Rev. Mater. 4 (2019) 269–285. https://doi.org/10.1038/s41578-019-0097-0.

[7] → H. Mu, F. Hu, R. Wang, J. Jia, Shuang Xiao, Effects of in-situ annealing on the electroluminescence performance of the Sn-based perovskite light-emitting diodes prepared by thermal evaporation, J. Lumin. 226 (2020) 117493. https://doi.org/10.1016/j.jlumin.2020.117493.

[8] → M.L. Lai, T.Y.S. Tay, A. Sadhanala, S.E. Dutton, G. Li, R.H. Friend, Z.-K. Tan, Tunable near-infrared luminescence in tin halide perovskite devices, J. Phys. Chem. Lett. 7 (2016) 2653–2658. https://doi.org/10.1021/acs.jpclett.6b01047.

[9] → C.M. Wolff, P. Caprioglio, M. Stolterfoht, D. Neher, Nonradiative Recombination in Perovskite Solar Cells: The Role of Interfaces, Adv. Mater. 31 (2019) 1902762. https://doi.org/10.1002/adma.201902762.

[10] → J. Chantana, Y. Kawano, T. Nishimura, A. Mavlonov, Q. Shen, K. Yoshino, S. Iikubo, S. Hayase, T. Minemoto, Impact of Auger recombination on performance limitation of perovskite solar cell, Sol. Energy. 217 (2021) 342–353. https://doi.org/10.1016/j.solener.2021.02.018.

[11] → B. Delley, A scattering theoretic approach to scalar relativistic corrections on bonding, Int. J. Quantum Chem. 69 (1998) 423–433. https://doi.org/10.1002/(SICI)1097-461X(1998)69:3<423::AID-QUA19>3.0.CO;2-2.

[12] → N. Troullier, J.L. Martins, Efficient pseudopotentials for plane-wave calculations, Phys. Rev. B. 43 (1991) 1993–2006. https://doi.org/10.1103/PhysRevB.43.1993.